

## Gebiss: an ImageJ plugin for the specification of ground truth and the performance evaluation of 3D segmentation algorithms

Kriston-Vizi *et al.*

SOFTWARE

Open Access

# Gebiss: an ImageJ plugin for the specification of ground truth and the performance evaluation of 3D segmentation algorithms

Janos Kriston-Vizi<sup>1,4\*</sup>, Ng Wee Thong<sup>1</sup>, Cheok Leong Poh<sup>1</sup>, Kwo Chia Yee<sup>1</sup>, Joan Sim Poh Ling<sup>2</sup>, Rachel Kraut<sup>2</sup> and Martin Wasser<sup>1,3</sup>

## Abstract

**Background:** Image segmentation is a crucial step in quantitative microscopy that helps to define regions of tissues, cells or subcellular compartments. Depending on the degree of user interactions, segmentation methods can be divided into manual, automated or semi-automated approaches. 3D image stacks usually require automated methods due to their large number of optical sections. However, certain applications benefit from manual or semi-automated approaches. Scenarios include the quantification of 3D images with poor signal-to-noise ratios or the generation of so-called ground truth segmentations that are used to evaluate the accuracy of automated segmentation methods.

**Results:** We have developed Gebiss; an ImageJ plugin for the interactive segmentation, visualisation and quantification of 3D microscopic image stacks. We integrated a variety of existing plugins for threshold-based segmentation and volume visualisation.

**Conclusions:** We demonstrate the application of Gebiss to the segmentation of nuclei in live *Drosophila* embryos and the quantification of neurodegeneration in *Drosophila* larval brains. Gebiss was developed as a cross-platform ImageJ plugin and is freely available on the web at <http://imaging.bii.a-star.edu.sg/projects/gebiss/>.

## Background

The widespread use of automated fluorescent confocal microscopy has resulted in a significant role for image analysis in modern quantitative biology. Quantitative features such as the number of cells or fluorescent intensity of subcellular organelles have become crucial for the elucidation of many biological and pharmaceutical hypotheses ranging from cell biology to anticancer drug development in various organisms such as *Caenorhabditis elegans* [1], *Drosophila melanogaster* [2-4] and even rodent models [5]. With the advent of three-dimensional (3D) optical sectioning of confocal microscopes and green fluorescent protein (GFP) as an expression marker [6], spatial distribution of cellular organelles can be studied. Histone tagged with fluorescent protein (e.g. GFP) [7] allow the observation of

DNA distribution in living cells. Recent innovations in light sheet microscopy enabled the study of the spatio-temporal organisation of nuclei in whole zebrafish and *Drosophila* embryos [8-10]. A vast amount of visual information is acquired in automated microscopy. Some of the extracted features are less sensitive to the precision of segmentation, such as the number of objects and their location based on centroid coordinates. Other, biologically important features such as shape or volume require a more precise segmentation.

Mechanisms of cell cycle regulation can be elucidated by live cell imaging and subsequent automated quantification of nuclei in intact organisms [11]. The living *Drosophila* embryo provides an attractive experimental system for the study of mitosis, where nuclei can be observed *in situ* [12].

Neurodegeneration is another biological phenomenon of intense interest that has been subjected to extensive study in *Drosophila* models, but for which there are few quantitative cell biological readouts. Generalized brain

\* Correspondence: [dmcbjkr@ucl.ac.uk](mailto:dmcbjkr@ucl.ac.uk)

<sup>1</sup>Bioinformatics Institute, Agency for Science, Technology and Research (A\*STAR), 30 Biopolis Street 07-01 Matrix, 138671, Singapore  
Full list of author information is available at the end of the article

neurodegeneration has been studied in *blue cheese (bchs) Drosophila* mutants [13], where ubiquitinated protein accumulation and a failure of degradative trafficking pathways have been implicated [14,15]. Kumarasamy et al. [16] determined by quantitative automated multivariate analysis of wide field fluorescence images that the degenerative phenotype was accompanied by changes in the size and distribution of lysosomal compartments within neuronal termini.

Loss of motor neurons has been documented in the third instar larval nervous system of *bchs* mutants, as well as superficial observations of smaller ventral ganglion size by confocal microscopy [13].

Image segmentation is an important step in the image processing workflow that is extensively applied in fluorescence microscopy. During segmentation foreground pixels are separated from background pixels. The use of machine segmentation (MS) in automatic image cytometry enables the measurement of cellular features in a high throughput fashion. However an automated imaging workflow cannot fully supplant the expertise of a trained biologist to detect and evaluate phenotypes. In a previous report, poorly-segmented cells were identified by eye in the framework of a high-content screening imaging pipeline [17]. Each of the authors of the report independently reviewed an equal fraction of the test image set, classifying into well-segmented and poorly-segmented qualitative groups using subjective criteria. Segmentation performance evaluation is still not common in cell-based high-content screening. Subjective descriptive terms such as “reasonably conformed perimeter” can serve well to train classifiers evaluating segmentations qualitatively and find features resistant (intensity-based features) or prone (morphology-based features) to imprecise cellular segmentation [17]. Besides “good” and “poor” segmentation, a quantitative evaluation can answer questions such as “how good” or “how poor” a machine segmentation algorithm is. The first step towards achieving such a quantitative evaluation is building a segmentation dataset that contains only well-segmented objects.

Performance evaluation methods can be divided into analytical and empirical groups, where the former investigates the algorithm directly and the latter judges it through the quality of the image segmentation. The empirical discrepancy method uses an ideal or expected segmentation result to objectively quantify the performance of an algorithm [18]. This concept takes into account the difference between an automatically segmented and a reference image and is generally used for practical image processing performance evaluation in real applications, where the accuracy of segmentation is the primary concern [19-23]. This approach produces easily interpretable results and is useful to perform a

quantitative comparison of different segmentation algorithms. However, such a reference, or ground truth (GT) dataset creation is generally considered as a labour-intensive step [24], where human intuition or judgment makes an expected objective evaluation to be influenced by subjective factors. The GT is defined as a reference data set that acts as the gold standard in segmentation evaluation. In the context of image segmentation, the GT can be represented in various formats that are created manually or semi-automatically by human experts. Contours represent regions of interest, while labelled 2D and 3D images are the most comprehensive format that include all pixels and voxels of detected image objects. In specialised applications such as nuclear segmentation, the GT is encoded in the form of centroids [10,25]. A designer of an image analysis system has an array of often task-specific machine segmentation choices, where the GT is the “correctly” segmented image, which is needed for objective numerical evaluation of those algorithms. Since there is no unique universal segmentation ground truth, against which machine segmentation results can be compared, a human expert must create a perceptually consistent GT. Currently, there is no dedicated software tool to evaluate segmentation quality. A number of programs have been developed to segment and visualise 3D optical image stacks automatically or interactively. The potential software packages ranges from the commercially available Imaris (Bitplane AG, Zurich Switzerland), Definiens Developer XD (Definiens AG, Munich Germany) and Matlab (Mathworks, Natick USA) to open source alternatives as Cellprofiler [26], the Segmentation Editor plugin under ImageJ [27]/Fiji [28] and ITK-SNAP [29]. However, the use of these applications are limited in 3D segmentation performance metrics [30].

Here, we present a software for manual 3D segmentation and segmentation performance evaluation: Gebiss (Ground Truth Editing and Benchmarking for Image Stack Segmentation). Gebiss was developed as an ImageJ [27] plugin. We used Gebiss to assess the neurodegenerative state of *Drosophila* mutants by measuring brain volumes. Such a phenotypic readout would permit us to test the effects of pharmacologic or genetic interventions that may affect the severity of the phenotype. Gebiss [31] was applied to the analysis of over 5000 single images from different 3D image datasets.

## Implementation

Gebiss was developed as an ImageJ plugin to help the biologist to generate a ground truth. The source code availability, platform independence and wide developer base made NIH ImageJ [27] (Figure 1a) an optimal environment for a ground truth creation and benchmarking application. Gebiss leverages ImageJ's core

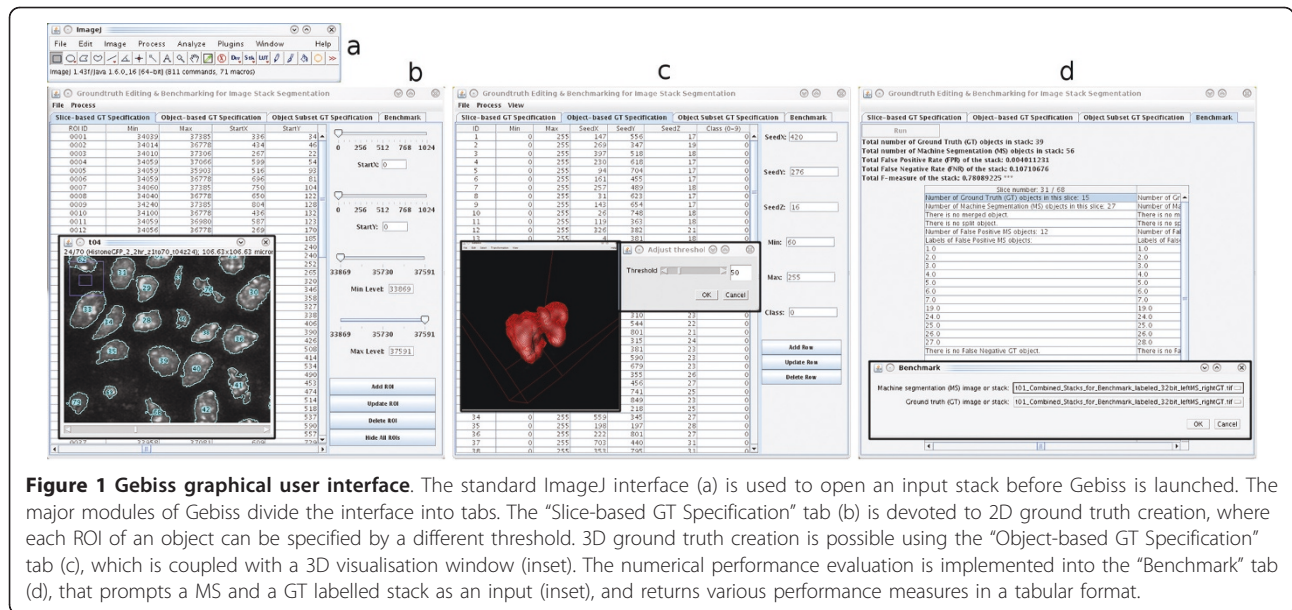


**Figure 1 Gebiss graphical user interface.** The standard ImageJ interface (a) is used to open an input stack before Gebiss is launched. The major modules of Gebiss divide the interface into tabs. The “Slice-based GT Specification” tab (b) is devoted to 2D ground truth creation, where each ROI of an object can be specified by a different threshold. 3D ground truth creation is possible using the “Object-based GT Specification” tab (c), which is coupled with a 3D visualisation window (inset). The numerical performance evaluation is implemented into the “Benchmark” tab (d), that prompts a MS and a GT labelled stack as an input (inset), and returns various performance measures in a tabular format.

capabilities such as easy installation, opening and saving in a wide range of image formats, such as Image Cytometry Standard ICS [32], uncompressed and ZIP-compressed TIFF stack or Zeiss LSM by the plugin OME LOCI Bio-Formats [33]. The graphical user interface of Gebiss (Figure 1b-d) was developed using the Swing toolkit for Java and its simple design guides the user along the workflow. Formerly an unsettled issue, memory allocation is not limited anymore. Both the current versions of Java and ImageJ are able to handle 64-bit platforms and > 4 GB RAM.

Besides ImageJ, Gebiss requires a Java3D installation for spatial visualisation. This can be done easily by following the steps of Benjamin Schmid’s guide. An alternative to the standard ImageJ is Fiji [28] which contains Java3D as part of a package. The Gebiss installation itself consists of downloading gebiss.jar and biImageJ3DViewer.jar from <http://imaging.bii.a-star.edu.sg/projects/gebiss/> and copying those into the “plugins” folder of ImageJ or Fiji, after which a “Gebiss” submenu appears automatically in the Plugins menu. Gebiss uses Jarek Sacha *ij-plugins Toolkit* that can be freely downloaded from <http://ij-plugins.sourceforge.net/> or version 1.4.1 can be found at the project web folder that must be copied into the “plugins” folder of ImageJ or Fiji.

Gebiss is run after an 8, or 16-bit greyscale microscopic image stack is opened. The spatial voxel dimensions can be imported either automatically from an ICS, TIFF, or LSM stack header, or otherwise can be set manually in ImageJ. Gebiss provides a function to set and save voxel depth enabling the storage and repeated retrieval of a value over several imaging sessions.

The methodology is illustrated with examples of live, wild type *Drosophila melanogaster* embryonic nuclei monitored with GFP histone H2A variant (H2Av-GFP) in various phases of the cell cycle. The confocal microscopic image stacks of the anterior part of the embryo were captured by a Zeiss LSM 5 DUO microscope.

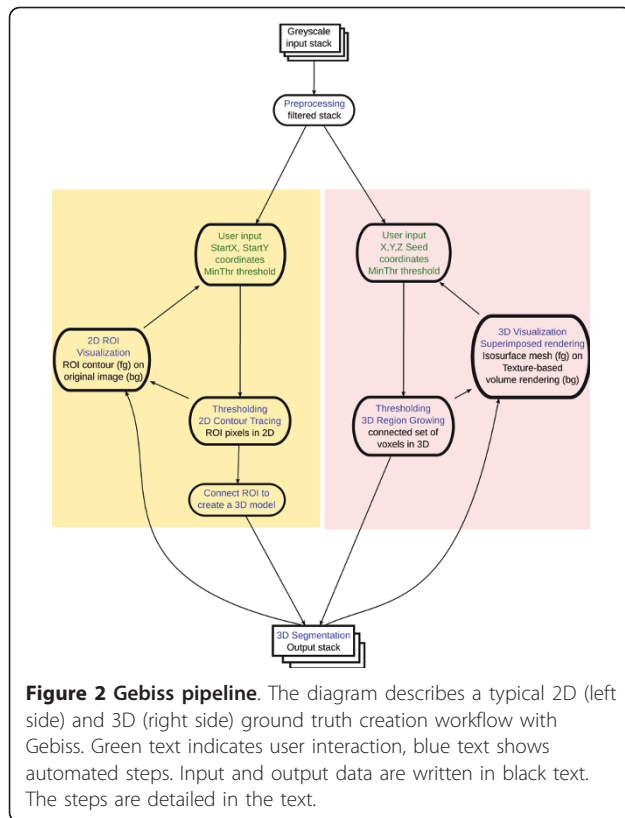
**Gebiss workflow**

The generation of a labelled ground truth image stack in Gebiss can be achieved through: i) segmenting each 2D ROI of a spatial object, ii) 3D segmentation of a spatial object or segmenting a group of spatial objects (Figure 2). The labelled GT stack can be saved and used to benchmark an arbitrary machine segmentation. Each original microscopic image stack is smoothed by applying a 3 pixel radius (7 × 7 pixel window sized) two dimensional median filter.

**2D slice-based GT creation workflow**

In the course of a slice-based segmentation (left side section of the flowchart in Figure 2), each optical slice of a spatial object can be segmented individually using different threshold values if necessary. The resulting ROIs can effectively exclude otherwise merged segmentation artefacts. Inspired by Michael M. Miller’s SegmentingAssistant plugin and using ImageJ’s core Wand tool class [34], each ROI is defined by four parameters: StartX, StartY, a minimum ( $\theta_{min}$ ) and a maximum intensity ( $\theta_{max}$ ) threshold value.

While SegmentingAssistant makes 2D local segmentation much easier and precise compared with a manual “freehand selection”, there was room for improvement. For example, sliders are not perfect for StartX, StartY selection in order to assign several points in an image.



A slider is not optimal to set  $\theta_{min}$  when the typical step is too small to be set by dragging the slider. Also, the parameter load and save functions were missing. Earlier the binary mask and labelled stack creation was complicated, as it required the combined use of ROI Manager and the 3D object counter [35] plugin.

Several features were built in Gebiss to improve productivity. StartX and StartY coordinates can be assigned by a single mouse click on the original image and  $\theta_{min}$  can be changed by rolling the mouse middle scroll wheel in intensity steps of 20 and 50 when combined with Shift or Ctrl key respectively. The parameter  $\theta_{max}$  is set to the brightest intensity value of the image by default, and requires adjustment in rare cases. The algorithm searches in the right direction until a pixel is found with an intensity falling into the range of  $[\theta_{min}, \theta_{max}]$ . Following that, it traces the contour of the 2D object in a clockwise direction. However, the resulting ROI is calculated by using the median filtered intensity values, which are invisible to the user. Superimposed on the original image, users are guided with continuous visual feedback as the contours are updated. Using the GUI of the Slice-based GT Specification tab (Figure 1b), the optimal StartX, StartY,  $\theta_{min}$  and  $\theta_{max}$  values are stored in a parameter database for each object, where they can be updated, deleted or invoked to create a binary and a labelled stack.

The 2D slice-based GT creation workflow is flexible enough to allow the use of multiple threshold values per 3D object if needed. At the same time, the reuse of the stored parameters of an object in the present optical slice enables faster processing of the consecutive slice. The latter approach assumes that the StartX, StartY and  $\theta_{min}$  parameters of the object ROI in the previous slice gives a correct contour. If not, the values can be adjusted to fit on the given contour.

### 3D object-based GT creation workflow

Gebiss is able to visualise 3D-thresholded foreground voxels as an isosurface superimposed on background voxels with original intensity. This double rendering feature can be switched on by checking in the Add isosurface submenu in the View menu of Gebiss, which appears when the tab is activated.

After an image stack is opened with ImageJ and Gebiss is started, 3D connected objects can be segmented interactively (Figure 2) by using the tab “Object-based GT Specification” (Figure 1c). Each 3D object is segmented individually by a seeded 3D region growing algorithm [36] originally implemented as ij-plugins Toolkit version 1.2 by Jarek Sacha. The Connected threshold region growing segmentation algorithm requires five parameters specified by the user: the x, y, z coordinates of a seed pixel as well as a minimum ( $\theta_{min}$ ) and a maximum intensity threshold value. Following the right side section of the flowchart in Figure 2, the seed pixel coordinates are defined on the image stack window by a single Ctrl plus left mouse key click on a bright fluorescent region (where intensity greater than  $\theta_{min}$ ) of a given object. The  $\theta_{min}$  is defined immediately after the seed selection.

To provide the user with 3D visual information to find the optimal  $\theta_{min}$ , a customized version of Benjamin Schmid’s ImageJ 3D Viewer plugin [37] was implemented into Gebiss. In order to simultaneously visualise background and foreground, Gebiss superimposes two 3D renderings. Background voxels are visualised by texture-based volume rendering using brightness-corrected fluorescent intensities. Foreground voxels are added forming a semi-transparent, red coloured isosurface mesh that allows the user to observe simultaneously both the interior and the exterior of the object. The default maximum intensity threshold value is 255 for images with a dark background and a bright foreground. The user selects an optimal  $\theta_{min}$  value in the “Adjust threshold...” window (Figure 1c). In the case of *Drosophila* embryos such a  $\theta_{min}$  value is low enough to include all heterochromatin regions and chromosome arms but high enough to exclude free histone and lipid droplets. By dragging the threshold slider, a 10-15 slice thick 3D mesh of a typical nucleus is rendered. The image can be freely rotated in 3D and zoomed using the mouse and

the middle wheel. The whole rotating 3D virtual environment can be recorded as an animated movie using ImageJ's AVI writer plugin.

An automated light attenuation compensation in GT creation is offered by a dual thresholding function implemented under the tab "Object Subset GT Specification". There are cases where the signal-to-noise ratio would allow the segmentation of a stack with a global threshold, though the light attenuation requires the use of a higher threshold value for deeply located objects. In this module two different thresholds are applied to objects located in shallower and deeper axial depth. The user is prompted for a data file containing the x, y, z seed coordinates of each object, a threshold value for the shallower and a second threshold value for the deeper objects as well as the demarcation z slice number that separates the shallow and deep slices. The x, y, z seed data file is generated using the 3D object counter [35] plugin. Even if its global thresholding segmentation produces imprecise contours in such cases, the derived object centroids are saved in a data file that serves as an x, y, z seed input file. This Gebiss module applies a 3D region growing segmentation using shallower or deeper  $\theta_{min}$  to the objects according to their z centroid value. In practice it is done as follows. A separation slice is set up at a certain depth. All nuclei are segmented by a 3D region growing algorithm. Those nuclei whose centroid's z parameter (the depth of the centroid point) is above the separation slice are segmented by a user-determined threshold value. Those nuclei whose centroid's z parameter is below the separation slice are segmented by a different threshold value.

#### **GT contour visualisation**

The requirement of human supervision for GT creation in any system may require an optional high level check. Fast and precise visualisation is achieved by the superimposition of all GT ROI contours on the original images. An ImageJ macro was created which uses a binary GT and original microscopic greyscale stacks as input files (see additional file 1: "ImageJ macro for GT contour visualisation"). The binary stack must be inverted (i.e. black foreground objects on a white background), and the original greyscale stack must be converted to RGB format. The macro automatically draws all segmented object contours on each of the original slices, visualising both the foreground and background pixels (see additional file 2: "3D GT contour visualisation"), therefore any missing 2D ROI or 3D object can be detected at the object level. At pixel level, false negatives such as unsegmented chromosome arms and false positives such as attached free histones or lipid droplets can be recognised easily. Any further GT ROI adjustment can be done by the respective Gebiss steps. The isosurface 3D rendering of a labelled stack can reveal falsely merged GT objects.

#### **Benchmarking workflow**

For segmentation performance evaluation, the most useful measures are precision, recall (sensitivity) and F-measure. All of those measures need the quantification of true positive (tp), false positive (fp) and false negative (fn) class labels defined by the four outcomes of the relation between the predicted class and the actual class.

The value of *precision* is calculated as  $p = \frac{tp}{tp + fp}$ , thus it depends on the number of false positives. Fewer false positives result in a precision value closer to 1. Similarly, the number of false negatives affect the *recall* value, that is calculated as  $r = \frac{tp}{tp + fn}$ , which is closer to 1 when the number of false negatives is low. The *F-measure* is expressed as  $F = \frac{2pr}{p + r}$ , and it evaluates the performance

of a machine segmentation in a single value as the harmonic mean of precision and recall. The closer the F-value is to 1, the better the given MS is. A ground truth segmentation contains neither any false positive nor any false negative pixel, therefore  $p_{GT} = 1$ ,  $r_{GT} = 1$  and  $F_{GT} = 1$ . In the context of segmentation, the performance evaluation can be quantified at two levels: object level and pixel level.

At the object level, the object number of MS and its deviation from that of the GT is calculated. The "object" term refers to either a 2D foreground region of interest (ROI) composed of 4 or 8-connected pixels or a 3D body composed of 18 or 26-connected foreground voxels. Ideally, each GT object matches an MS object resulting in a one-to-one correspondence. The machine segmentation may result in a false positive object that does not occur in GT or a false negative, missing one that does occur in GT. An MS object may be split (one-to-many correspondence) if more than one MS object matches a GT object or merged (many-to-one correspondence) if more than one GT object matches an MS object.

At pixel level, the correspondence between the foreground and the background region is quantified. Each segmented pixel or volumetric pixel (voxel) can be classified as true positive, false positive, true negative (tn) or false negative. The number of tp, fp, tn and fn pixels are counted, and precision, recall and F-measure are calculated for a 3D stack or a 2D slice. The benchmarking module requires a labelled MS and a labelled GT stack as input files. It has a numerical output (Figure 1d) and a visual output that is shown in additional files 3 and 4 ("Numerical output of the Gebiss benchmarking module" and "Visual output of the Gebiss benchmarking module", respectively). The numerical output displays benchmark measures for the whole stack as well as each

individual slice. For the whole stack, the number of GT and MS objects are indicated at object level. Several well-established performance metrics [30] are in use (precision, recall and F-measure), that are derived from the confusion matrix. The precision, recall and F-measure are calculated at the pixel level. For each individual slice, the module calculates the number of GT and MS objects as well as the number and label of merged and split objects (if any). This feature enables the precise identification of the slice where ROI merge occurs. The number and label of occurrent false positive MS and false negative GT objects are also calculated.

## Results and Discussion

Gebiss is a tool for semi-automated 3D image segmentation which can be used either as a ground truth in performance evaluation or in image quantification. We applied it to different biological datasets. A good example is the process of nuclear division in the early *Drosophila* embryo, which has been extensively described. Precise nuclear segmentation is critical in quantifying this aspect of embryonic development. Contour finding in nuclear segmentation can be challenging as lipid droplets surround and attach to nuclei. The condensed chromosomes are often surrounded by a cloud of free histone that impedes the segmentation of a specific surface. This problem also applies to all deeply located nuclei in a stack where laser attenuation leads to poor signal-to-noise ratio. Additionally, the contrast of a whole image stack may be low owing to the uniform intensity of foreground and background pixels. Gebiss offers the biologist diverse ways to overcome these obstacles.

### Case study 1: Nucleus segmentation in embryogenesis 2D segmentation of embryonic nuclei

One of the objectives of this study is measuring the volume of nuclei. To measure the precise nuclear volume, segmentation must correctly separate an attached lipid droplet from a discrete one that locates in the close proximity of a nucleus. Gebiss can be first used to measure the volume of nuclei marked by H2Av-GFP. To quantify nuclear features like size, shape, number, etc., it is necessary to separate the two classes of nuclear histone and cytoplasmic histone. A lipid droplet-specific marker, such as Nile Red dye [38], effectively allows lipid droplet segmentation and separation from the nuclei, but using the less organelle-specific H2Av-GFP it is still possible to create a precise ground truth segmentation. The top row of Figure 3 illustrates the 2D slice segmentation of a nucleus optical section from the original image (Figure 3a) through a contour resulting from an incorrect (Figure 3b) and a correct (Figure 3c)  $\theta_{min}$  value. Figure 3d shows the final

segmented image of the nucleus. Decreasing the  $\theta_{min}$  value for a whole 3D object is usually not helpful to detach a lipid droplet artefact because 3D shrinking leads to the loss of the correct spherical shape of an interphase nucleus. Consequently, we disconnected a lipid droplet by the  $\theta_{min}$  reduction of only certain 2D nuclear slices while we preserved the correct nuclear shape.

The H2Av-GFP intensity gradient is often low between a distinct lipid droplet and a nucleus before the histone assembles into the chromatin (Figure 4). This complicates the 3D gradient-based segmentation. The intensity variation inside a nucleus can exceed that of the variation between the nucleus and a distinct lipid droplet nearby (Figure 4c).

The repeated use of a certain parameter set in multiple ROI slices allows accelerated GT creation, however it points out the intrinsic limitations of the method when used for segmentation of a spatial object. Certain ROIs can overlap each other and can be omitted inadvertently as a result of parameter reuse. Since only one slice is shown at a time and the thresholding parameter can be adjusted arbitrarily, the resulting contour can be flickery over slices of low contrast stacks. Finding the optimal thresholds of the top and bottom slices and the contours can be difficult in such cases. 3D segmentation alleviates those shortcomings.

To determine whether machine segmentation artefacts cause remarkable changes in measured volumes, dividing nuclei were traced throughout mitosis. The high H2Av-GFP intensity gradient inside a prophase nucleus led to unfilled holes in segmenting a syncytial blastoderm nucleus with MS (Figure 5), resulting in different volume measurement between GT and MS segmentation.

### 3D nucleus segmentation to detach free histone

The individual and manual specification of several thousand ROI contours of a segmented image stack is a flexible, but slow and laborious method, prone to human error. 3D object-based segmentation speeds up the process and the user can semi-automatically segment a whole object by using a single threshold. A typical nucleus spreads over ~10 to ~30 slices, thus by choosing a 3D object-level  $\theta_{min}$  many ROIs can be segmented simultaneously. Selecting an optimal  $\theta_{min}$  is the main user task after the x, y, z coordinates of a seed pixel are chosen. The middle row image series of Figure (3e, f, g, h) guides the viewer through the process via the 3D segmentation of a metaphase nucleus. The volume-rendered 3D view (Figure 3e) shows a heterochromatin region surrounded by free histone from below that has been spuriously attached because of an incorrectly low  $\theta_{min}$  value (Figure 3f). The optimal  $\theta_{min}$  removes the free histone and at the same time preserves the shape of

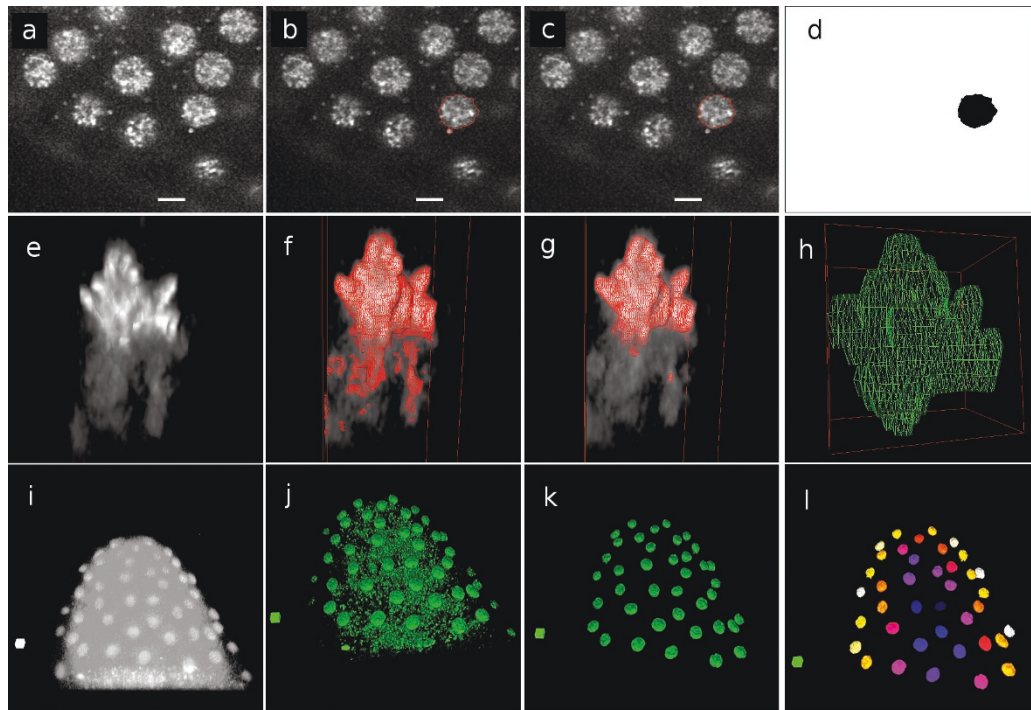


**Figure 3 Comparison between original and segmented data.** Original data (a, e, i). Segmentation with incorrect (b, f, j) and correct (c, g, k) threshold values. Segmentation results (d, h, l). **Top row:** To separate a lipid droplet from a nucleus, a 2D slice of the original image (a) is segmented through a contour resulted by an incorrect (b) and a correct  $\theta_{min}$  value (c), finally showing the segmented image (d). The scale bars indicate  $5 \mu\text{m}$ . **Middle row:** 3D segmentation of a metaphase nucleus (e) with (f) and without (g) free histone attachments and a 3D mesh isosurface representation of the segmented slices (h). The dimensions of the bounding cube are  $7.1 \mu\text{m} \times 8.8 \mu\text{m} \times 13.6 \mu\text{m}$  (e-g),  $10.5 \mu\text{m} \times 12.6 \mu\text{m} \times 7.8 \mu\text{m}$  (h). **Bottom row:** Low contrast image stack (i) segmentation leads to adding visually significant false positive voxels by using a global threshold (8-bit threshold value  $\theta = 44$ ) (j). It is segmented correctly by 3D object-based segmentation (k), resulting in a labelled stack (l). The regular cubes in the left side of the panels (i)-(l) indicate  $50 \mu\text{m}^3$ .

the mitotic nucleus (Figure 3g), resulting in the correctly segmented optical slices (Figure 3h).

As a result, nuclei are segmented in interphase and various mitotic phases such, as prophase, metaphase,

anaphase A, anaphase B and telophase, respectively (See Figure 6 and additional files 5a-f). This module also enables the user to distinguish between axial and lateral 3D object fusions (unpublished data).

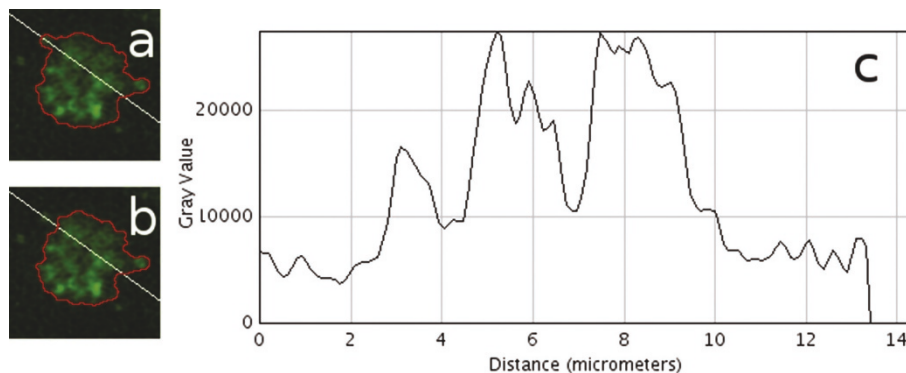
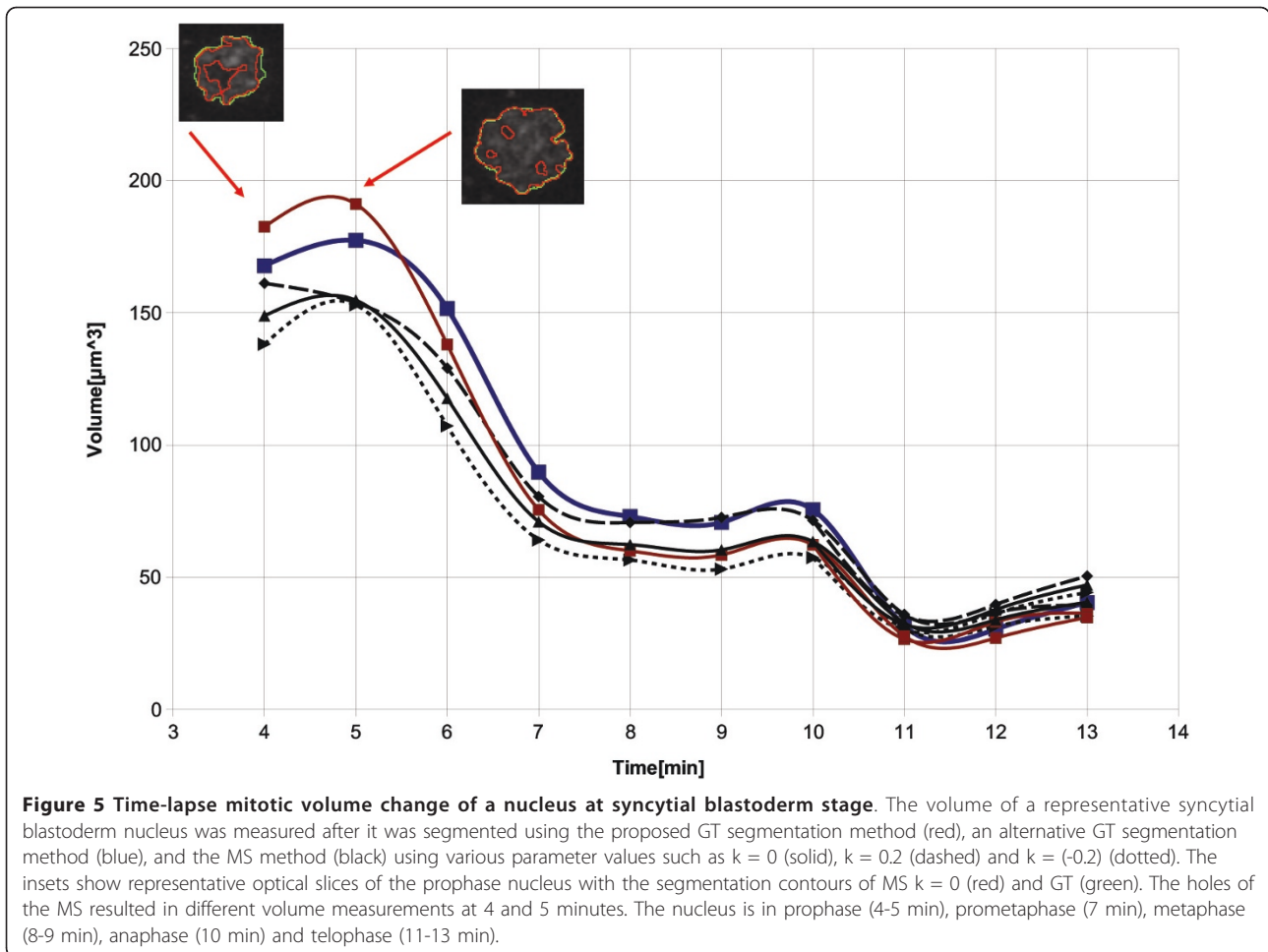


**Figure 4 Lipid droplet and nucleus segmentation.** Low H2Av-GFP intensity gradient in an optical section between a distinct lipid droplet and a nucleus. (a)-(b) 2D segmentation contours using 16-bit  $\theta_{min} = 9131$  (a) and  $\theta_{min} = 9574$  (b). The lipid droplet locates in the upper left region of the image, intersected by the white profile line. Size of the images (a) and (b):  $10.8 \mu\text{m} \times 10.8 \mu\text{m}$ . (c) Greyscale intensity profile plot. The intensity values of the lipid droplet and the nucleus range between 2 -  $4 \mu\text{m}$  and 5 -  $10 \mu\text{m}$  respectively.





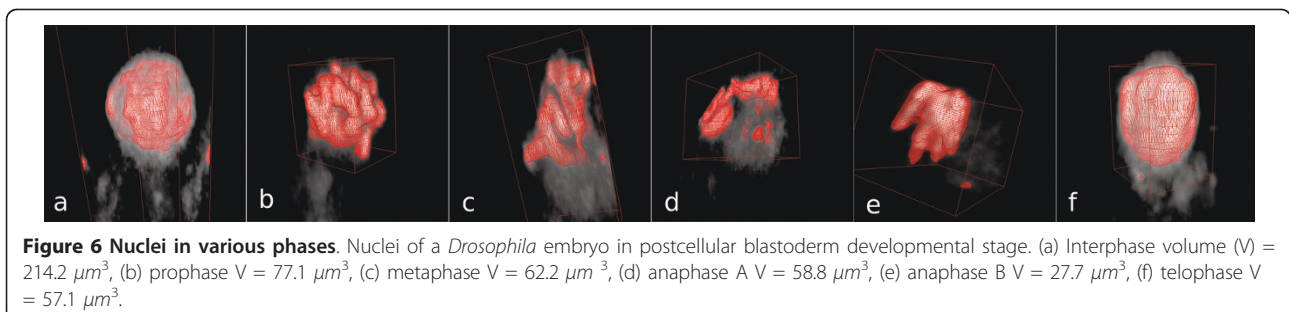
### Segmentation of a low contrast embryonic image stack

The brightly stained central yolk mass of the *Drosophila* embryo is still overlapping with the periplasm during nuclear cycle 10 in the syncytial blastoderm, which lasts until the the depth of yolk-free periplasm increases dramatically at the expense of the central yolk region in nuclear cycle 13 [39]. As a result, the contrast of a whole image stack becomes low owing to the uniform intensity of foreground and background pixels (Figure 3i). Global thresholding (Figure 3j) gives visually

unacceptable segmentation results. The individual 3D object-based GT specification is a segmentation method that was able to remove the noise around the nuclei (Figure 3k) and create a labelled image stack (Figure 3l).

### Case study 2: 3D segmentation of Drosophila brain

In order to provide a quantitative measurement of the strength of phenotypes resulting from *bchs* gain-of-function or loss-of-function mutations, Lim and Kraut first made use of the percentages of larval RP2 motor neuron



loss through the immunostaining of GFP-expressing RP2 motor neurons [13]. However, we sought to make the phenotypic measurement faster and more quantitative. Therefore in this study, we have measured the brain volumes of different late third instar *bchs* mutant larvae (Figure 7) by labelling the dissected whole larval brain with rhodamine-conjugated phalloidin, which recognizes F-actin. The *bchs58* allele is a nonsense mutation that encodes for a truncated protein, while *Df(2L)clot7* is a deficiency on the left arm of chromosome 2. As shown in Table 1, both genotypes of *bchs58/Df(2L)clot7* and homozygous *bchs58* have a 15% to 17% reduction in the brain volumes of the third instar larvae, when compared with the brains of the larvae from the genetic background of the *bchs58* allele mutants (YW).

This reduction in *bchs* mutant brain volume is statistically significant (unpaired Student's t test,  $p < 0.001$ ) as compared with the YW control and it is in agreement with our previous phenotypic quantification method of RP2 motor neuron loss [13]. In addition, the smaller reduction in *bchs* mutant brain volume at the third instar larval stage in comparison with an estimated 40% reduction in adult *bchs* mutant brain volume [14] may be explained by the longer duration of the adult stage which allows progressive neurodegeneration to occur. From this brain volumetric analysis, there is no significant difference between the two different *bchs* null alleles, *bchs58/Df(2L)clot7* and homozygous *bchs58*, indicating that the *bchs58* allele is, as expected from earlier studies [13], acting as a null allele with respect to *bchs'*

**Table 1 Comparison of mutant Drosophila brain volumes**

Genotype 1	Genotype 2	p-value	volume difference <sup>a</sup> [%]
C155/yw	C155/+; EP2299/+	< 0.001	+ 14.6%
YW	<i>bchs58/bchs58</i>	< 0.001	- 16.9%
YW	<i>bchs58/Df(2L)clot7</i>	< 0.001	- 15.5%
<i>bchs58/bchs58</i>	<i>bchs58/Df(2L)clot7</i>	0.641	NA
C155/+; EP2299/+	<i>bchs58/bchs58</i>	< 0.001	- 10.3%
C155/+; EP2299/+	<i>bchs58/Df(2L)clot7</i>	< 0.01	- 8.8%

Using Gebiss we show that both *bchs* null mutant combinations of *bchs58/Df(2L)clot7* and homozygous *bchs58* have a reduction in the brain volumes of third instar larvae, when compared with the background genotype YW brains as a control. <sup>a</sup>The difference in brain volume of Genotype 2 in comparison with Genotype 1 as the reference control. NA: Non-applicable.

effect on brain volume. The reduction in brain volume of *bchs* null larvae is consistent with the earlier observation made in adult animals [14] and suggests that the overall level of degeneration in the larval brain can be assessed using the Gebiss method of volumetric analysis.

Conversely, over-expression of the *bchs* using the EP2299 line in conjunction with the C155 *Gal4* driver in the central nervous system resulted in an increase of 14.6% brain volume when compared with the control, C155/yw. Together with the observed shrinkage in brain volume of loss of function in *bchs* mutants, these results suggest that *Bchs* may have some role in determining cellular volume and/or proliferation in the brain.

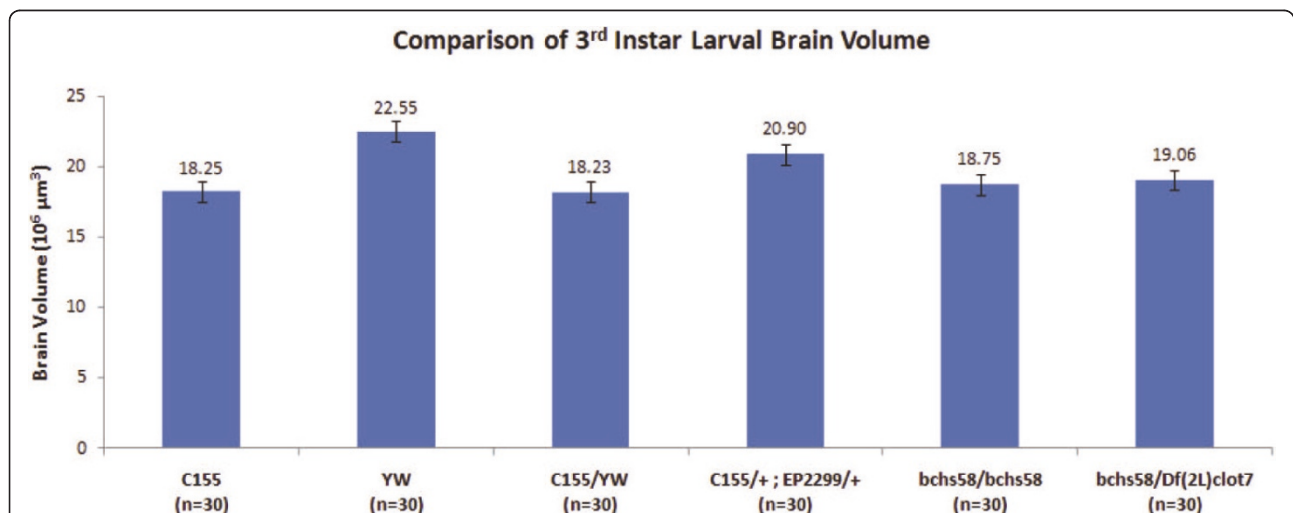


**Figure 7 Comparison of mutant Drosophila brain volumes.** Both genotypes of *bchs58/Df(2L)clot7* and homozygous *bchs58* have a reduction in the brain volumes of third instar larvae compared to the wild type stock yw. The *Gal4* driver line C155 and C155 crossed to yw were used as additional controls for C155 crossed to the *Bchs*-overexpressing EP2299 line.

### Segmentation performance evaluation

To test the performance of 3D segmentation methods, we applied six different automated MS algorithms to segment *Drosophila* brain stacks: Yen's method [40], Rényi entropy [41], Li's minimum cross entropy [42], Huang's fuzzy thresholding [43], Ridler and Calvard's iterative Isodata method [44] and Otsu's thresholding [45] (Figure 8). The segmentation result image stacks can be found in additional file 6: "Visual segmentation performance evaluation". All algorithms are implemented under ImageJ by Gabriel Landini, and compute a global threshold from the stack image to segment the stack, with the limitation that only 8-bit image stacks are supported. The advantage is that no manual parameter entry is required. The computed threshold is lower, equal to or higher than that of ground truth.

Therefore, the segmented brain stacks resulted in greater, equal to or smaller volumes, respectively. MS volumes greater than GT lack any false negative pixels, thus leading to  $r = 1$  recall in the case of Li and Huang segmentation. Conversely, MS volumes smaller than GT lack any false positive pixels, thus resulting in  $p = 1$  precision at Yen, Rényi, Isodata and Otsu methods.

The 8-bit image stacks had histograms shifted to darker voxel intensities. We used the global threshold value 23 to create GT (Figure 9). However, global threshold values between 19 and 28 gave F-measures 0.95 and above, indicating that the brain contour was not sharp.

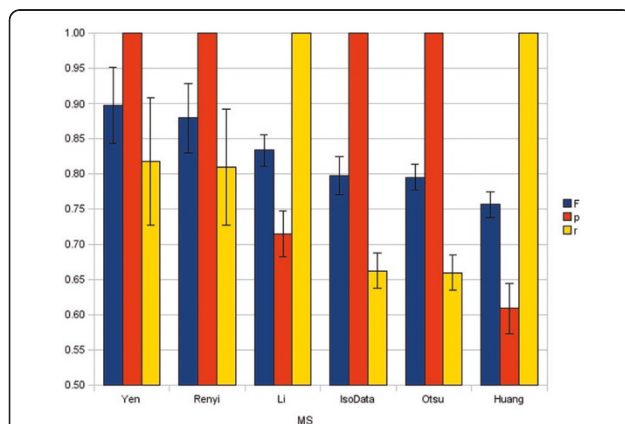


**Figure 8 Machine segmentation performances on *Drosophila* brain segmentation.** Performance evaluation of six MS algorithms segmenting *Drosophila* brain stacks ( $n = 5$ ). All algorithms calculate a single global threshold. When that threshold is smaller than that of GT, there will not be any false positive voxel which leads to 100% precision ( $p = 1$ , orange) in case of Yen, Rényi, IsoData and Otsu methods. When the MS threshold is calculated to be larger than that of GT, there will not be any false negative voxel resulting in 100% recall ( $r = 1$ , yellow) in the case of the Li and Huang methods. F-measure values are represented by the blue bars. Error bars represent standard deviation.

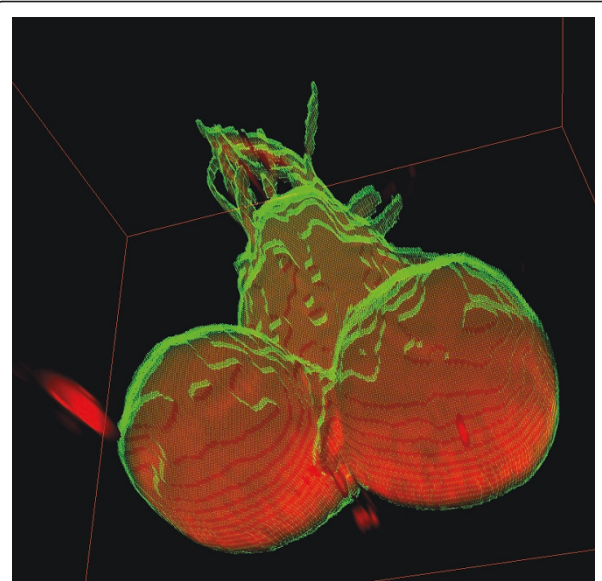


**Figure 9 Bchs58/c17 neurodegenerative mutant *Drosophila* brain GT segmentation visualised in 3D.** *Drosophila* central nervous system segmented voxels (green isosurface mesh) superimposed on original voxel intensities (red volume rendering), the volume is  $22.38 \times 10^6 \mu\text{m}^3$ .

Huang's fuzzy thresholding belongs to the algorithms that uses Shannon's entropy function and segments based on attribute similarity. Measuring the similarity between the original and the binary image stack, it determined the threshold by minimising the measure of fuzziness. Including average foreground and background intensities, the algorithm computed a low MS threshold value in our dark stacks, resulting in numerous false positive voxels and the poorest mean F-measure, which is still above 0.75.

Although widely used popular methods in imaging, the performance of the clustering-based segmentation algorithms of Isodata and Otsu performed less well than the others. Both methods assume that a stack has two grey intensity maxima and partition the histogram of an image stack into two classes, based on intra-class variance minimisation and inter-class variance maximisation. The Otsu method searches for the optimal threshold globally, whereas the Isodata does this locally, thus these methods result in almost identical thresholds. These algorithms work optimally with a bimodal histogram, where the number of voxels are similar in both the foreground and the background class. One reason for the weaker segmentation performance is that the number of black background voxels affect the threshold computed by those two algorithms. Also the background and foreground intensity modes are not separated sharply in the histograms of our brain stacks.

Among the tested MS algorithms, the three entropy-based segmentation methods performed the best. Li's method is based on cross-entropic thresholding. It has a significantly reduced computational requirement compared with the exhaustive search method but it tends to calculate a lower threshold value than that of GT.

We found that Yen's method and Rényi's entropy performed the best among the algorithms that were tested. The two algorithms are similar and performed similarly well. Both belong to Shannon-entropy maximisation-based segmentation methods [46], originating from one-dimensional entropic thresholding introduced by Pun in 1981 [47].

## Conclusions

In this paper, we present Gebiss, a new software for quantitative 3D segmentation performance evaluation. Gebiss was designed to be a productive and user friendly tool for ground truth creation, and it includes a benchmarking module that objectively evaluates a 3D segmentation. The package was developed as a plugin for ImageJ, is platform independent and can be freely downloaded from <http://imaging.bii.a-star.edu.sg/projects/gebiss/>. Gebiss was successfully used in various biological tasks.

## Availability and requirements

**Project name:** Gebiss

**Project home page:** <http://imaging.bii.a-star.edu.sg/projects/gebiss/>

**Operating system:** platform independent

**Programming language:** Java

**Other requirements:** ImageJ 1.43 m or higher, Java 1.6.0\_16 or higher

**License:** GNU GPLv3

## Additional material

**Additional file 1: ImageJ macro for GT contour visualization.** ImageJ macro file in Unix text format. Before running, it requires two input image stacks to be opened. An original image stack, converted into RGB format and renamed as "orig" as well as its matching binary stack renamed as "bin" with black foreground and white background pixels. For the macro operation see the text.

**Additional file 2: 3D GT contour visualization.** Compressed, spatially calibrated RGB image stack that can be opened by standard ImageJ. GT segmentation contours (green) are superimposed on the original, low contrast image slices. By simultaneously visualising both the foreground and background pixels, the user can easily check the ground truth segmentation. The stack's xyz dimensions are  $133.3 \mu\text{m} \times 133.3 \mu\text{m} \times 29.9 \mu\text{m}$ .

**Additional file 3: Numerical output of the Gebiss benchmarking module.** Quantitative machine segmentation benchmark results demonstrated on a low contrast image stack of a *Drosophila* embryo in syncytial blastoderm developmental stage, containing 68 slices. Data in columns represents the evaluation of each optical slices. The slice numbers are indicated in the table header, followed by measures of each individual slices respectively: number of GT and MS objects (if any),

number and labels of merged and split objects (if any), number and labels of false positive and false negative MS objects (if any).

**Additional file 4: Visual output of the Gebiss benchmarking module.** Compressed, spatially calibrated image stack. It can be opened using ImageJ. It horizontally combines the MS (left) and the GT (right) 32-bit labelled stacks in an easily comparable manner. Demonstrated on a low contrast image stack containing 68 slices.

**Additional file 5: Nuclei in various phases.** Six animated GIF movies in one compressed file. After uncompressing, those can be opened by ImageJ or an internet browser. The movies show nuclei of a *Drosophila* embryo in postcellular blastoderm developmental stage. (a) Interphase volume  $V = 214.2 \mu\text{m}^3$ , (b) prophase  $V = 77.1 \mu\text{m}^3$ , (c) metaphase  $V = 62.2 \mu\text{m}^3$ , (d) anaphase A  $V = 58.8 \mu\text{m}^3$ , (e) anaphase B  $V = 27.7 \mu\text{m}^3$ , (f) telophase  $V = 57.1 \mu\text{m}^3$ .

**Additional file 6: Visual segmentation performance evaluation.** ZIP compressed, spatially calibrated, segmented binary image stacks, that can be opened by standard ImageJ. The images represent the 3D segmentation results discussed in the section "Segmentation performance evaluation". File names indicate the machine segmentation that resulted the given stack.

## Acknowledgements

The authors thank Wee Choo Puah for the *Drosophila* embryo image acquisition, Chinta Rambabu for his constructive comments, Derek Smith and Daniel Bosch Ibáñez for their critical revision of the manuscript, Wayne Rasband for ImageJ and all the developers of the ImageJ plugins that were used in this paper.

## Author details

<sup>1</sup>Bioinformatics Institute, Agency for Science, Technology and Research (A\*STAR), 30 Biopolis Street 07-01 Matrix, 138671, Singapore. <sup>2</sup>School of Biological Sciences, Nanyang Technological University, Singapore. <sup>3</sup>Department of Biological Sciences, National University of Singapore, Singapore. <sup>4</sup>Translational Research Resource Centre, Laboratory for Molecular Cell Biology, Medical Research Council, University College London, London, UK.

## Authors' contributions

JKV carried out the design and implementation of the software, analysed the images and wrote the manuscript. NWT participated in the implementation of the software, CLP coordinated the implementation of the software, KCY participated in the implementation of the software, JSPL carried out the *Drosophila* brain experiment, RK conceived and coordinated the *Drosophila* brain experiment, MW conceived and coordinated the study. All authors read and approved the final manuscript.

Received: 12 November 2010 Accepted: 13 June 2011

Published: 13 June 2011

## References

1. Brenner S: **The Genetics of Caenorhabditis Elegans.** *Genetics* 1974, 77:71-94.
2. Agard DA, Hiraoka Y, Shaw P, Sedat JW: **Chapter 13 Fluorescence Microscopy in Three Dimensions.** In *Fluorescence microscopy of living cells in culture Part B Quantitative fluorescence microscopy-imaging and spectroscopy, Volume 30 of Methods in Cell Biology.* Edited by: Taylor DL, Wang YL. Academic Press; 1989:353-374, 374a, 375-377.
3. Fritsch C, Ploeger G, Arndt-Jovin D: **Drosophila under the lens: imaging from chromosomes to whole embryos.** *Chromosome Research* 2006, 14(4):451-464.
4. Kirilly D, Gu Y, Huang Y, Wu Z, Bashirullah A, Low BC, Kolodkin AL, Wang H, Yu F: **A genetic pathway composed of Sox14 and Mical governs severing of dendrites during pruning.** *Nature Neuroscience* 2009, 12:1497-1505.
5. Seluanov A, Hine C, Azpurua J, Feigenson M, Bozzella M, Mao Z, Catania KC, Gorbunova V: **Hypersensitivity to contact inhibition provides a clue to**

- cancer resistance of naked mole-rat. *Proceedings of the National Academy of Sciences* 2009, **106**(46):19352-19357.
6. Piston DW, Patterson GH, Knobel SM: **Chapter 3: Quantitative Imaging of the Green Fluorescent Protein (GFP)**. In *Green Fluorescent Proteins, Volume 58 of Methods in Cell Biology*. Edited by: Sullivan KF, Kay SA. Academic Press; 1998:31-48.
  7. Leach T, Mazzeo M, Chotkowski H, Madigan J, Wotring M, Glaser R: **Histone H2AZ is widely but nonrandomly distributed in chromosomes of *Drosophila melanogaster***. *J Biol Chem* 2000, **275**(30):23267-23272.
  8. Huiskens J, Swoger J, Del Bene F, Wittbrodt J, Stelzer E: **Optical sectioning deep inside live embryos by selective plane illumination microscopy**. *Science* 2004, **305**(5686):1007.
  9. Keller P, Stelzer E: **Quantitative in vivo imaging of entire embryos with Digital Scanned Laser Light Sheet Fluorescence Microscopy**. *Current Opinion in Neurobiology* 2008, **18**(6):624-632.
  10. Keller P, Schmidt A, Wittbrodt J, Stelzer E: **Reconstruction of zebrafish early embryonic development by scanned light sheet microscopy**. *Science* 2008, **322**(5904):1065.
  11. Mora-Bermúdez F, Gerlich D, Ellenberg J: **Maximal chromosome compaction occurs by axial shortening in anaphase and depends on Aurora kinase**. *Nat Cell Biol* 2007, **9**(7):822-831.
  12. Hiraoka Y, Agard D, Sedat J: **Spatial arrangement of homologous chromosomes during anaphase in early embryos of *Drosophila melanogaster* studied by three-dimensional fluorescence microscopy**. *Bioimaging* 1997, **5**(4):183-193.
  13. Lim A, Kraut R: **The *Drosophila* BEACH family protein, blue cheese, links lysosomal axon transport with motor neuron degeneration**. *J Neurosci* 2009, **29**(4):951-963.
  14. Finley KD, Edeen PT, Cumming RC, Mardahl-Dumesnil MD, Taylor BJ, Rodriguez MH, Hwang CE, Benedetti M, McKeown M: **Blue cheese mutations define a novel, conserved gene involved in progressive neural degeneration**. *J Neurosci* 2003, **23**(4):1254-1264.
  15. Simonsen A, Birkeland HCG, Gillooly DJ, Mizushima N, Kuma A, Yoshimori T, Slagsvold T, Brech A, Stenmark H: **Alfy, a novel FYVE-domain-containing protein associated with protein granules and autophagic membranes**. *J Cell Sci* 2004, **117**(18):4239-4251.
  16. Kumarasamy S, Wang Y, Viswanathan V, Kraut R: **Multivariate profiling of neurodegeneration-associated changes in a subcellular compartment of neurons via image processing**. *BioData Mining* 2008, **1**:10.
  17. Hill A, LaPan P, Li Y, Haney S: **Impact of image segmentation on high-content screening data quality for SK-BR-3 cells**. *BMC Bioinformatics* 2007, **8**:340.
  18. Zhang YJ: **A review of recent evaluation methods for image segmentation**. *Signal Processing and its Applications, Sixth International Symposium on 2001* 2001, **1**:148-151.
  19. Lee SJ, Chung SY, Park RH: **A comparative performance study of several global thresholding techniques for segmentation**. *Computer Vision, Graphics, and Image Processing* 1990, **52**(2):171-190.
  20. Unnikrishnan R, Pantofaru C, Hebert M: **A Measure for Objective Evaluation of Image Segmentation Algorithms**. *Computer Vision and Pattern Recognition-Workshops, 2005 CVPR Workshops IEEE Computer Society Conference on 2005*, **34**.
  21. Unnikrishnan R, Pantofaru C, Hebert M: **Toward Objective Evaluation of Image Segmentation Algorithms**. *Pattern Analysis and Machine Intelligence, IEEE Transactions on 2007*, **29**(6):929-944.
  22. Crevier D: **Image segmentation algorithm development using ground truth image data sets**. *Comput Vis Image Underst* 2008, **112**:143-159.
  23. Hodneland E, Bukoreshtliev N, Eichler T, Tai XC, Gurke S, Lundervold A, Gerdes HH: **A Unified Framework for Automated 3-D Segmentation of Surface-Stained Living Cells and a Comprehensive Segmentation Evaluation**. *Medical Imaging, IEEE Transactions on 2009*, **28**(5):720-738.
  24. Huang Q, Dom B: **Quantitative methods of evaluating image segmentation**. *Image Processing, 1995 Proceedings, International Conference on 1995*, **3**:53-56.
  25. Santella A, Du Z, Nowotschin S, Hadjantonakis AK, Bao Z: **A hybrid blob-slice model for accurate and efficient detection of fluorescence labeled nuclei in 3D**. *BMC Bioinformatics* 2010, **11**:580.
  26. Carpenter A, Jones T, Lamprecht M, Clarke C, Kang I, Friman O, Guertin D, Chang J, Lindquist R, Moffat J, Golland P, Sabatini D: **CellProfiler: image analysis software for identifying and quantifying cell phenotypes**. *Genome Biology* 2006, **7**(10):R100.
  27. Abramoff M, Magalhaes P, Ram S: **Image processing with ImageJ**. *Biophotonics International* 2004, **11**(7):36-43[http://rsbweb.nih.gov/ij/].
  28. Schindelin J: **Fiji is just ImageJ - batteries included**. *Proceedings of the ImageJ User and Developer Conference 6-7 November 2008; Luxembourg* Centre de Recherche Public Henri Tudor; 2008, 99-104.
  29. Yushkevich PA, Piven J, Cody Hazlett H, Gimpel Smith R, Ho S, Gee JC, Gerig G: **User-Guided 3D Active Contour Segmentation of Anatomical Structures: Significantly Improved Efficiency and Reliability**. *Neuroimage* 2006, **31**(3):1116-1128.
  30. Fawcett T: **An introduction to ROC analysis**. *Pattern Recognition Letters* 2006, **27**(8):861-874.
  31. Kriston-Vizi J: **An ImageJ plugin for the benchmarking of 3D segmentation algorithms and the specification of ground truth datasets**. *Proceedings of the ImageJ User and Developer Conference 6-7 November 2008; Luxembourg* Centre de Recherche Public Henri Tudor; 2008, 200.
  32. Dean P, Mascio L, Ow D, Sudar D, Mullikin J: **Proposed standard for image cytometry data files**. *Cytometry* 1990, **11**(5):561-569.
  33. Swedlow JR, Goldberg J, Brauner E, Sorger PK: **Informatics and Quantitative Analysis in Biological Imaging**. *Science* 2003, **300**(5616):100-102.
  34. Burger W, Burge M: *Digital image processing: an algorithmic introduction using Java* Springer-Verlag New York Inc; 2007.
  35. Bolte S, Cordelieres F: **A guided tour into subcellular colocalization analysis in light microscopy**. *Journal of microscopy* 2006, **224**(3):213-232.
  36. Adams R, Bischof L: **Seeded region growing**. *Pattern Analysis and Machine Intelligence, IEEE Transactions on 1994*, **16**(6):641-647.
  37. Schmid B, Schindelin J, Cardona A, Longair M, Heisenberg M: **A high-level 3D visualization API for Java and ImageJ**. *BMC Bioinformatics* 2010, **11**:274.
  38. Cermelli S, Guo Y, Gross SP, Welte MA: **The Lipid-Droplet Proteome Reveals that Droplets Are a Protein-Storage Depot**. *Current Biology* 2006, **16**(18):1783-1795.
  39. Foe V, Alberts B: **Studies of nuclear and cytoplasmic behaviour during the five mitotic cycles that precede gastrulation in *Drosophila* embryogenesis**. *Journal of Cell Science* 1983, **61**:31.
  40. Yen JC, Chang FJ, Chang S: **A new criterion for automatic multilevel thresholding**. *Image Processing, IEEE Transactions on 1995*, **4**(3):370-378.
  41. Kapur J, Sahoo P, Wong A: **A new method for gray-level picture thresholding using the entropy of the histogram**. *Computer vision, graphics, and image processing* 1985, **29**(3):273-285.
  42. Li C, Lee C: **Minimum cross entropy thresholding**. *Pattern Recognition* 1993, **26**(4):617-625.
  43. Huang LK, Wang MJJ: **Image thresholding by minimizing the measures of fuzziness**. *Pattern Recognition* 1995, **28**:41-51.
  44. Ridler TW, Calvard S: **Picture Thresholding Using an Iterative Selection Method**. *Systems, Man and Cybernetics, IEEE Transactions on 1978*, **8**(8):630-632.
  45. Otsu N: **A Threshold Selection Method from Gray-Level Histograms**. *Systems, Man and Cybernetics, IEEE Transactions on 1979*, **9**:52-66.
  46. Sezgin M, Sankur B: **Survey over image thresholding techniques and quantitative performance evaluation**. *J Electron Imaging* 2004, **13**:146-168.
  47. Pun T: **Entropy thresholding: A new approach**. *Computer, Graphics and Image Processing* 1981, **16**:210-239.

doi:10.1186/1471-2105-12-232

**Cite this article as:** Kriston-Vizi et al.: Gebiss: an ImageJ plugin for the specification of ground truth and the performance evaluation of 3D segmentation algorithms. *BMC Bioinformatics* 2011 **12**:232.